

Weak gravitational lensing shear estimation with METACALIBRATION for the *Roman* High-Latitude Imaging Survey

Masaya Yamamoto,^{1*} M. A. Troxel,¹ Mike Jarvis,² Rachel Mandelbaum,³ Christopher Hirata,^{4,5,6} Heyang Long,^{4,5} Ami Choi,⁷ and Tianqing Zhang³

¹*Department of Physics, Duke University, Durham, NC, 27708*

²*Department of Physics and Astronomy, University of Pennsylvania, Philadelphia, PA 19104, USA*

³*McWilliams Center for Cosmology, Department of Physics, Carnegie Mellon University, Pittsburgh, Pennsylvania 15213, USA*

⁴*Center for Cosmology and Astro-Particle Physics, The Ohio State University, 191 West Woodruff Avenue, Columbus, OH 43210, USA*

⁵*Department of Physics, The Ohio State University, 191 West Woodruff Avenue, Columbus, OH 43210, USA*

⁶*Department of Astronomy, The Ohio State University, 140 West 18th Avenue, Columbus, OH 43210, USA*

⁷*Department of Physics, California Institute of Technology, 1200 E. California Blvd., Pasadena, California 91125, USA*

Accepted XXX. Received YYY; in original form ZZZ

ABSTRACT

We investigate the performance of the METACALIBRATION shear calibration framework using simulated imaging data for the *Nancy Grace Roman* Space Telescope (*Roman*) reference High-Latitude Imaging Survey (HLIS). The weak lensing program of *Roman* requires the mean weak lensing shear estimate to be calibrated within about 0.03%. To reach this goal, we can test our calibration process with various simulations and ultimately isolate the sources of residual shear biases in order to improve our methods. In this work, we build on the HLIS image simulation pipeline to incorporate several more realistic processing-pipeline updates. We show the first METACALIBRATION results for six deg² of the simulated reference HLIS and compare them to measurements on simpler, faster *Roman*-like image simulations. We neglect the impact of blending of objects. We find in the simplified simulations, METACALIBRATION can calibrate shapes to within $m = (-0.01 \pm 0.10)\%$. When applied to the current most-realistic version of the simulations, the precision is much lower, with estimates of $m = (-0.76 \pm 0.43)\%$ for joint multi-band multi-epoch measurements and $m = (-1.13 \pm 0.60)\%$ for multi-band coadd measurements. These results are all consistent with zero within $1-2\sigma$, indicating we are currently limited by our simulated survey volume. Further work on testing the shear calibration methodology is necessary at the precision of the *Roman* requirements, in particular in the presence of blending. Current results demonstrate, however, that METACALIBRATION can work on undersampled space-based *Roman* imaging data at levels comparable to requirements of current weak lensing surveys.

Key words: gravitational lensing: weak – cosmology: observations – techniques: image processing

1 INTRODUCTION

Since the formulation of the standard cosmological model, most observational evidence has been consistent with the flat Λ -CDM model in which the contents of the universe are mostly in the dark sector (Planck Collaboration et al. 2020; Gil-Marín et al. 2020; Tamone et al. 2020; Asgari et al. 2021; DES Collaboration et al. 2022; Brout et al. 2022). Within this sector, dark energy accounts for the accelerating expansion of the universe (e.g., Riess et al. 1998; Perlmutter & Riess 1999) and the combination of dark energy and dark matter are responsible for the observed growth of large-scale structure (Kilbinger 2015; Dodelson 2017). The growth of structure can be studied by measuring quantities that are sensitive to the way light rays are deflected by intervening mass in the Universe, a physical phenomenon called gravitational lensing. “Weak” gravitational lensing causes a slight distortion to intrinsic galaxy shapes called shear.

By detecting millions of these gravitationally lensed galaxies and computing their ensemble shear, we can explore the dark matter density and the amplitude of matter fluctuation in the universe (e.g., Bartelmann & Schneider 2001). Measuring these quantities eventually helps us learn about the history of the development of the large-scale structure in the universe. For that reason, weak lensing is one of the most powerful probes in current and near-future imaging surveys to constrain cosmological parameters with high precision.

Due to the subtlety in the lensing effect and its systematics-dominant nature in the weak regime (Mandelbaum 2018), observational efforts have been challenging. Over the past decade, large international collaborations such as the Dark Energy Survey¹ (DES: The Dark Energy Survey Collaboration 2005), the Hyper Suprime-Cam Subaru Strategic Program² (HSC: Aihara et al. 2018), and the

¹ <http://www.darkenergysurvey.org/>

² <http://hsc.mtk.nao.ac.jp/ssp/>

* E-mail: masaya.yamamoto@duke.edu

Kilo-Degree Survey³ (KiDS: [de Jong et al. 2013](http://kids.strw.leidenuniv.nl/)) have been successful at constraining the cosmological parameters, and the precision in calibrating the estimates of shear from the shapes of distant galaxies has reached a few percent ([Mandelbaum et al. 2018](http://sci.esa.int/euclid); [Gatti et al. 2020](http://www.lsst.org); [MacCrann et al. 2020](https://roman.gsfc.nasa.gov); [Giblin et al. 2021](https://roman.gsfc.nasa.gov)). As we observe more area on the sky and develop better tools (observatories and algorithms), we detect more galaxies, and have already reached the point where statistical and systematic uncertainties are comparable. Thus, near-future Stage IV surveys ([Albrecht et al. 2006](http://www.lsst.org)) such as *Euclid*⁴ ([Laureijs et al. 2011](http://www.lsst.org)), the Vera C. Rubin Observatory Legacy Survey of Space and Time⁵ (*LSST*: [LSST Science Collaboration et al. 2009](http://www.lsst.org); [Ivezic et al. 2019](https://roman.gsfc.nasa.gov)), and the *Nancy Grace Roman* Space Telescope⁶ (*Roman*: [Spergel et al. 2015](https://roman.gsfc.nasa.gov)) require even better control of systematics. In order to understand the systematic uncertainties we face, we must develop realistic image simulations, apply existing shape measurement methods to the simulated images, and determine any potential residual systematic effects and build a strategy for modifying the calibration methodology to mitigate them.

Based on our current knowledge, systematic biases for weak lensing science, both observational and astrophysical, can occur at all stages of the imaging survey (e.g., [Mandelbaum 2018](http://sci.esa.int/euclid)). In particular, observational systematics can be due to:

- inhomogeneous observing strategy,
- atmospheric and instrumentation effects,
- post-processing pipelines such as image coaddition and object detection.

Conventionally, these observational systematic biases are characterized through a number of simulations and validation tests, and these propagate into uncertainties on the final mean galaxy shear we measure. We quantify this impact as shear calibration bias. Several shear calibration and bias mitigation efforts have been inspired by the outcomes of the Shear TEsting Programme (STEP; [Heymans et al. 2006](http://www.lsst.org); [Massey et al. 2007](http://www.lsst.org)), the GRavitational lEnsing Accuracy Testing challenges (GREAT; [Bridle et al. 2010](http://www.lsst.org); [Kitcing et al. 2013](http://www.lsst.org); [Mandelbaum et al. 2015](http://sci.esa.int/euclid)) and other image simulations work (e.g., [Hoekstra et al. 2017](http://sci.esa.int/euclid)), to meet the requirements for the current imaging surveys. In particular, one of the state-of-the-art self-calibration methods, METACALIBRATION ([Huff & Mandelbaum 2017](http://sci.esa.int/euclid); [Sheldon & Huff 2017](http://sci.esa.int/euclid)) has been shown to be able to substantially reduce the significance of shear bias. It has been confirmed that shear can be calibrated with METACALIBRATION at the few-percent level in DES ([Zuntz et al. 2018](http://www.lsst.org); [Gatti et al. 2020](http://www.lsst.org)), without accounting for galaxy blending and detection. Tackling the issue of blending/detection is one key step forward for the DES Y6 analysis and preparatory Rubin LSST work with the shear-dependent detection and calibration technique METADETECTION⁷ ([Sheldon et al. 2020](http://sci.esa.int/euclid); [Hoekstra et al. 2021](http://sci.esa.int/euclid)). While the major advantage of METACALIBRATION or METADETECTION is that they can be directly applied to real galaxy images without needing to rely on an ensemble calibration from image simulations, limitations for future surveys are not well-known.

One possible limitation might lie in the effect of undersampled images in space-based surveys like *Euclid* and *Roman*, which will

operate at their respective diffraction limits. The Point Spread Function (PSF) needs to be interpolated and estimated from well-sampled images to accurately deconvolve and measure shapes with, because the *Roman* PSF has a complex structure that cannot be captured in the original undersampled images. It is, therefore, necessary to build a robust strategy to reconstruct well-sampled images to estimate the PSF to allow unbiased shape measurement. Recently, [Kannawadi et al. \(2021\)](http://sci.esa.int/euclid) (hereafter K21) addressed this potential issue of the limitations of METACALIBRATION on undersampled images in *Euclid* image simulations. They found that for the *Euclid* mission the shear estimate with METACALIBRATION is biased by about 1%. It is mentioned that their result could be extended to the *Roman* mission due to similarities in the instruments and for *Roman* they predicted the multiplicative bias was more than 1%. They show that these effects can be mitigated using additional weighting kernels in the measurement.

In this work, we explore how METACALIBRATION performs using coadd images at higher resolution than the native resolution of the instrument, taking advantage of the dithering of images in the reference HLIS. We use an updated suite of image simulations specifically made for the *Roman* reference HLIS mission. Our work is based on the image simulation suite for the *Roman* Space Telescope developed by [Troxel et al. \(2021\)](http://sci.esa.int/euclid) (hereafter T21), where we render star and galaxy images using GalSim⁸ ([Rowe et al. 2015](http://www.lsst.org)). We describe several important updates to the simulation capabilities and realism following T21. We also implement for the first time METACALIBRATION using the simulated imaging within the T21 simulation suite, so that we can start to explore if the shear calibration goals of the HLIS for *Roman* ($m = 3.2 \times 10^{-4}$) ([Doré et al. 2018](http://sci.esa.int/euclid)) can be achieved with current METACALIBRATION implementations,⁹ or will require substantial additional development.

This paper is organized as follows. We first introduce the formalism of shear bias and image sampling relevant to the space-based surveys in Sec. 2. We then briefly discuss the simulation suite details we used and the updates we implemented for this project in Sec. 3. In Sec. 4, we show how coadditions of single exposure postage stamps are produced and how shape measurements are completed using METACALIBRATION. We present the galaxy catalog properties and calibration results for single-band and multi-band measurements in Sec. 5. Finally, in Sec. 6, we discuss how we will be able to constrain the shear bias better in terms of further updates in the image simulations and what we can conclude from this study.

2 BACKGROUND

In this section, we provide a brief introduction to image sampling defined through the Nyquist-Shannon Sampling Theorem, an overview of shear calibration bias within the context of weak lensing, and the METACALIBRATION formalism.

2.1 Image Sampling

Based on the Nyquist-Shannon Sampling Theorem, which states that in order to reconstruct an unbiased continuous band-limited function without a loss of information, the sufficient sample rate is twice the bandlimiting frequency per second. In the context of image

³ <http://kids.strw.leidenuniv.nl/>

⁴ <http://sci.esa.int/euclid>

⁵ <http://www.lsst.org>

⁶ <https://roman.gsfc.nasa.gov>

⁷ METADETECTION reduces a significant amount of shear-dependent detection bias by detecting objects after shearing a small region of the sky to measure the shear-dependent detection selection bias.

⁸ Version 2.3.1 was used. <https://github.com/GalSim-developers/GalSim>

⁹ We limit the study to METACALIBRATION for now, since we can extract unblended cutouts of objects in our simulations.

sampling, the criterion that the sample pixel spacing needs to satisfy is $p < \frac{1}{2u_{\max}}$ (u_{\max} is the maximum spatial bandlimiting frequency). Since the spatial bandlimiting frequency in an astronomical image is defined as

$$u_{\max} = \frac{1}{\lambda_{\min} N_f} \quad (1)$$

the sampling factor for a space telescope is defined as

$$Q = \frac{\lambda_{\min} N_f}{p}, \quad (2)$$

where λ_{\min} is the shortest wavelength of the incident light in each filter, N_f is the focal ratio of the telescope ($N_f = 7.8$ for *Roman*) and p is the pixel spacing of the sensor ($p = 10 \mu\text{m}$ for *Roman*) (Shapiro et al. 2013). An image with sampling factor $Q = 2$ is considered Nyquist-sampled and an image with sampling factor $Q < 2$ is undersampled. The image sampling for *Roman* are $Q=0.88, 1.08, 1.31$ for the J129, H158, and F184 bandpasses respectively.

2.2 Shear Calibration Bias

In the observation of weak lensing, we can quantify the bias associated with the shear recovery processes such as PSF estimation and shape measurement in image simulations. We call this shear calibration bias and we compute the deviations of the measured gravitational lensing shear γ from the input shear. Here we define the reduced shear $g \equiv \gamma/(1 - \kappa)$, and it is safe to approximate $\gamma \approx g$ in the context of cosmic shear. In the limit of weak lensing ($|\gamma| \ll 1, |\kappa| \ll 1$) and random intrinsic galaxy shapes, the ensemble average of ellipticities $\langle e \rangle$ of galaxy shapes is directly related to the reduced shear field g , and the estimated shear can be written as a linear model with multiplicative (m_i) and additive bias (c_i) as described in the equation below (Heymans et al. 2006; Huterer et al. 2006; Massey et al. 2007)

$$g_i^{\text{obs}} = (1 + m_i)g_i^{\text{true}} + c_i, \quad (3)$$

where $i=(1,2)$ are the two components representing an elliptical distortion, which can be derived from the major and minor axes, and g_i^{obs} is the two-component observed reduced shear after calibrations and g_i^{true} is the true shear. The bias can be introduced in places such as PSF modeling, blending, and the undersampling of the image (e.g., Mandelbaum 2018). Additionally, complex detector effects such as the brighter-fatter effect are potential sources of bias (Choi & Hirata 2020), while it has been shown that for *Roman* the effect of persistence will not be an issue (Lin et al. 2021). Qualitatively, if the recovered shear is biased by 1% ($m = 0.01$), from the cosmic shear power spectrum $S_8 = \sigma_8 \sqrt{\Omega_m}/0.3$ could be estimated to be biased about 1.5% in the final cosmology result. Thus, quantifying and correcting these biases before the real survey begins are extremely important.

2.3 METACALIBRATION Formalism

Here, we briefly summarize how METACALIBRATION (Huff & Mandelbaum 2017; Sheldon & Huff 2017) calibrates the biased measurement of galaxy ellipticities on the image stamps. Each stamp is defined to be an image cutout with one galaxy. METACALIBRATION creates one unsheared and four artificially-sheared galaxy stamps. Each is deconvolved with the input PSF, left unsheared or sheared with an additional gravitational shear of $\delta g = \pm 0.01$ in the two basis directions (g_1, g_2) and re-convolved with a new slightly larger isotropic, Gaussian PSF. We have chosen to use a Gaussian PSF

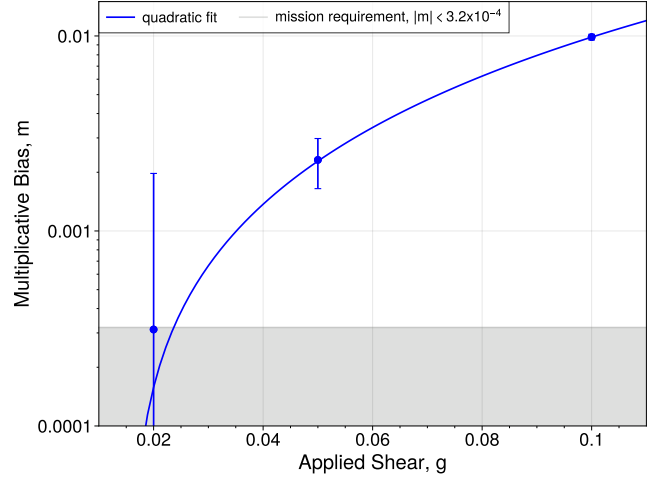


Figure 1. We show the recovered multiplicative bias on the shear as a function of the applied shear in our simplified simulations. The presented multiplicative bias is the average of m_1 and m_2 , and the grey shaded region represents the mission requirement. At first order, the METACALIBRATION algorithm only works for small input shears. The next order effect is seen as a quadratic dependence of the multiplicative shear bias on the applied shear (Sheldon & Huff 2017). A larger input shear increases the signal-to-noise of bias estimates, but to keep the non-linear effect small compared to requirements, we limit input shears to ± 0.02 .

since it simplifies the following (de)convolution operations and appears to be sufficient at our current testing precision. It will need to be verified that this continues to hold at the limit of the Roman requirements. METACALIBRATION works under the assumption that the input shear is small, otherwise the recovered shear would be biased without accounting for higher order terms. It is a balance to choose an input shear that results in higher S/N of the estimated shear bias and unbiased shear measurement. Figure 1 shows the performance as a function of input shear leading to the choice of input shear $g = \pm 0.02$.

After processing the images with METACALIBRATION and measuring the shapes, we have 5 shape catalogs for the five values of shear applied by METACALIBRATION. We can then compute the shear response from these catalogs and calculate the calibrated ensemble galaxy shears. The shear response can be understood as the change in objects' ellipticities with respect to the change in gravitational shear. Mathematically, the observed ellipticities, $e = (e_1, e_2)$, can be approximated using a Taylor expansion around the two-component shear, $g = 0$. Higher terms here can be dropped assuming the gravitational shear is small:

$$e = e|_{g=0} + \left. \frac{\partial e}{\partial g} \right|_{g=0} g + \dots \quad (4)$$

From this expression, the shear response matrix can be defined as

$$R_\gamma \equiv \left. \frac{\partial e}{\partial g} \right|_{g=0} = \begin{pmatrix} \partial e_1 / \partial g_1 & \partial e_2 / \partial g_1 \\ \partial e_1 / \partial g_2 & \partial e_2 / \partial g_2 \end{pmatrix}. \quad (5)$$

The ensemble mean of measured ellipticities $\langle e \rangle$ can then be computed. If the object selection cuts (e.g., S/N) are imposed when selecting the sample of galaxies for shear measurement, $\langle R \rangle = \langle R_\gamma \rangle + \langle R_s \rangle$, where $\langle R_s \rangle$ refers to the selection response

$$R_s \equiv \left. \frac{\partial \langle e^{\text{noshear}} \rangle}{\partial g} \right|_{g=0} \quad (6)$$

and corrects for selection bias. In this paper, all non-trivial object selection is done prior to image simulation, which prevents shear selection biases that arise due to object selection cuts imposed on the images; hence, $\langle R \rangle = \langle R_\gamma \rangle$ is a sufficient approximation.

Since we expect galaxies to be randomly oriented such that $\langle e \rangle|_{g=0} = 0$, we have a relationship between the measured ellipticities and the input shear in the simulations,

$$\langle e \rangle \approx \langle R \rangle \langle g \rangle. \quad (7)$$

In practice, we compute the mean shear response from the four sheared versions of the METACALIBRATION catalogs using the finite difference method.

$$\langle R_{ij} \rangle = \frac{\langle e_i^+ - e_i^- \rangle}{2\delta g_j}, \quad (8)$$

where e_i^+ and e_i^- are the i -th component of the galaxy ellipticity where positive (+) or negative (-) shear is applied in i -th direction.

The mean shear response is then used to get the METACALIBRATION-calibrated shears from the unsheared catalog. For individual objects, using Eqn. (3), we compare the input shear and the calibrated shapes to calculate multiplicative (m) and additive bias (c). We note that these shear biases are computed using only the diagonal term of the shear response in Eqn. (5).

3 SIMULATIONS

The base of our image simulations of the *Roman* Space Telescope is the *Roman* simulation suite¹⁰ developed by T21, which renders realistic galaxy and star images on 18 Sensor-Chip Assemblies (SCAs) of a 2.5×2.5 deg² patch of the sky following the observing strategy for the 5-year reference mission and Cycle 7 instrument specifications.¹¹ We begin by creating a truth catalog using the simulated galaxy distribution from the Buzzard simulation (DeRose et al. 2019), a photometric galaxy catalog sampled from the Cosmic Assembly Near-infrared Deep Extragalactic Legacy Survey (CANDELS; Grogin et al. 2011; Koekemoer et al. 2011; Hemmati et al. 2019), and a Milky Way simulation (Galaxia; Sharma et al. 2011) for star positions and magnitudes. Then, the following properties are assigned to each galaxy:

- positions (RA, Dec),
- flux within each *Roman* filter (F184/H158/J129/Y106),
- intrinsic galaxy shapes and random orientations,
- flux ratios of de Vaucouleurs bulge, exponential disk, and star-forming knots, and
- artificial gravitational lensing shears.

Positions are drawn from the galaxy density in the Buzzard simulation, while other properties are drawn randomly from realistic distributions, with intrinsic object properties following a distribution based on CANDELS data. Within four identical realizations of the simulation, we use four sets of gravitational shears $(e_1, e_2) = \{(+0.02, 0.00), (-0.02, 0.00), (0.00, +0.02), (0.00, -0.02)\}$. This approach helps us to reduce shape and measurement noise when taking the difference in recovered shapes to compute the multiplicative bias (Pujol et al. 2019).

The next step of the process is to create postage stamps and SCA

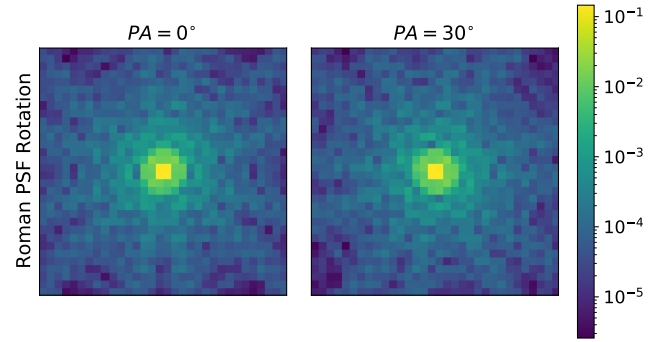


Figure 2. The rotation of the Roman PSF produced by the `galsim.roman` module. The position angle (PA) which determines the rotation of the focal plane is 0° (left) and 30° (right) clockwise. These are drawn for SCA=1 and H158 bandpass at a native pixel scale. The rotation of the PSF is particularly important when an object has multiple exposures. As more exposures are rotated relative to one another on the sky, the average impact of the PSF will be rounder. This will translate to a substantially less-elliptical coadd PSF.

images using `Galsim`. In this stage, the point-spread function (PSF) is convolved with the intrinsic galaxy light profile. Here, the *Roman* PSF is rendered using the `galsim.roman` module, which has implemented *Roman*-specific instrument properties such as the PSF and World Coordinate System (WCS) for a given telescope pointing, rotation angle, and SCA. The simulated detector effects were then added to the images in the following order: reciprocity failure, quantization, dark current, persistence, non-linearity, interpixel capacitance, read noise, and electron-to-ADU conversion (Mosby et al. 2020). These simulations have an achromatic PSF implementation, due to it being computationally infeasible to do a large chromatic simulation when the work began. For this analysis, we use isolated object cutouts for each object, so that effects related to blending can be ignored in this first study of METACALIBRATION for *Roman*.

After we generate the object stamps across all the SCAs and pointings, we create Multi-Epoch Data Structure (MEDS¹²; e.g., Jarvis et al. 2016) files in which each unique object dictionary contains information of all the exposures in which it appears in. These MEDS files are partitioned in a given Hierarchical Equal Area iso-Latitude Pixelisation (HEALPIX) of $n_{\text{side}} = 512$. They contain all objects that are located in that region of the sky partitioned according to HEALPIXEL¹³ (Górski et al. 2005; Zonca et al. 2019).

Once the objects are sorted in MEDS files, we pass these multiple exposures with the corresponding PSFs to `ngmix`¹⁴ to fit the galaxy shapes with the Gaussian mixture fitting method (Sheldon 2014). This shape measurement process produces shape catalogs from which the shear response is calculated with METACALIBRATION, and shear calibration bias can finally be computed.

3.1 Updates to Simulation Capabilities

In order to accomplish the science goals, and build and test weak lensing calibration pipelines for *Roman*, we have continued to update the realism of our image simulations. We have implemented and made updates to the following parts of the simulation framework to be able to better test shear calibration using METACALIBRATION.

¹⁰ https://github.com/matroxel/roman_imsim

¹¹ https://roman.gsfc.nasa.gov/science/Roman_Reference_Information.html

¹² Version 0.9.8 was used. <https://github.com/esheldon/meds>

¹³ <https://healpix.jpl.nasa.gov/>

¹⁴ Version 1.3.6 was used. <https://github.com/esheldon/ngmix>

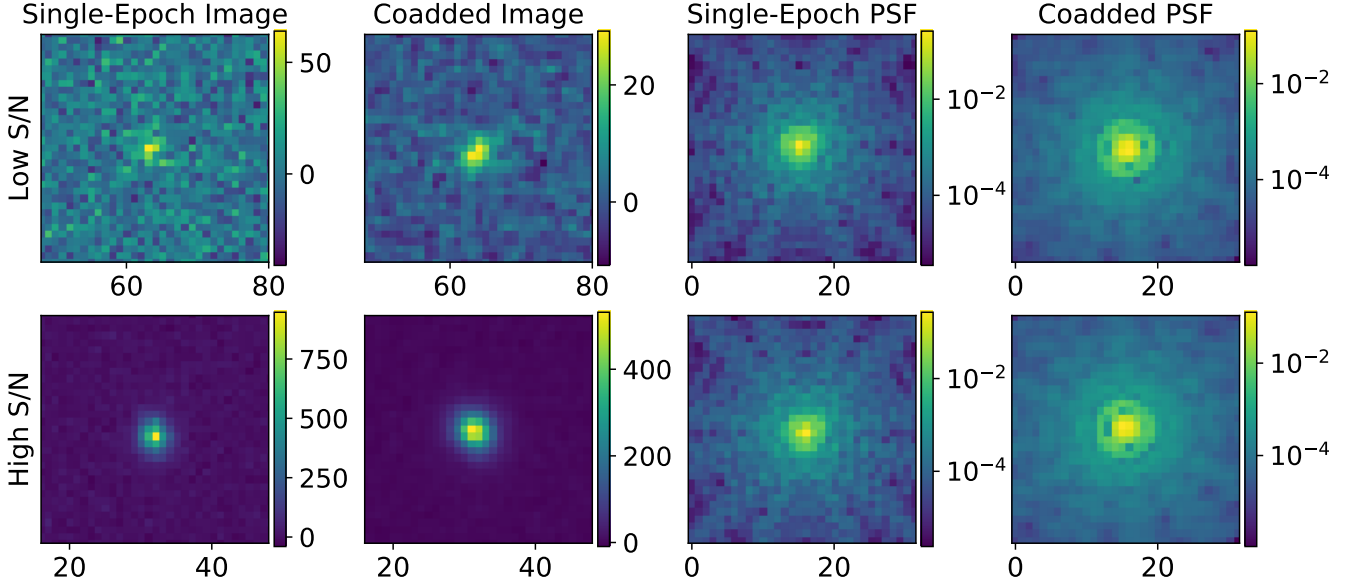


Figure 3. **Top Row:** the first observation of the single-epoch images and its coadded image, and the corresponding single-epoch and coadded oversampled PSF images for a galaxy with low signal-to-noise ratio ($S/N=20$ in a single-epoch image). **Bottom Row:** the same as above for a galaxy with high signal-to-noise ratio ($S/N=390$ in a single-epoch image). The H158 bandpass was used to represent images here. The single-epoch PSFs are almost identical, since there is no visually different feature for modeling them in different dithers and SCAs. There are two features to note here. One is how coaddition helps for low S/N objects, and the other feature is that the coadded PSFs look more isotropic than the single-epoch PSF due to different numbers of exposures.

- **Saturation Cuts:** We have implemented a pixel saturation limit of 100,000 electrons. This value is an expected pixel saturation level for *Roman* detectors, but in the next generation of the simulations we will use a more accurate pixel saturation limit measured directly from the flight detectors.

- **Rotation of the *Roman* PSF on the sky:** In the study by T21, the rotations of the *Roman* PSF with respect to the telescope rotation were not properly applied by the `galsim.roman` module. Since a non-rotating PSF produces an artificial preferred direction, which can translate to galaxy shapes through errors in the process of deconvolution, properly accounting for the averaging of the PSF orientation across exposures due to the survey dithering strategy is essential for a realistic shear calibration estimate. There has been an update in the `galsim.roman` module to correctly rotate the PSF given the WCS of the SCA in a given telescope pointing. Figure 2 shows an example of how the PSF for one SCA changes with the rotation angle of the telescope.

- **Single-band and multi-band Coadds:** We have used the postage stamp coadds (psc) algorithm¹⁵ to create coadditions of single-epoch postage stamps of individual objects. Coadds are usually performed to enhance the signal-to-noise ratio (S/N) of an image and mitigate the impact of measurement noise, while allowing for better sampling of the image if the overlapping images are dithered. However, it is challenging to create a robust, continuous coadd PSF model over an entire image. This is mitigated if we instead construct small, local coadds (at the size of an object postage stamp cutout in this work), which is a method also utilized in `METADETECTION`. If we take advantage of fitting an object in the coadd instead of fitting multiple images of each object in each filter, we can save a factor of

approximately six in computing time, since there are on average six exposures at any point on the sky in the reference survey. Additionally, coadding is one way to reduce the effect of the undersampling of the images since the coadd can be better sampled due to dithering. For these reasons, we explore utilizing this coadding scheme for the *Roman* galaxies. In future work, a coaddition algorithm could be used such as `IMCOM`¹⁶ (Rowe et al. 2011) that explicitly addresses the undersampling in a way that psc does not. The examples of the low and high S/N galaxy and PSF images for single-epoch and coadd are shown in Figure 3. The detailed overview of the coadd process in psc is described in in Sec. 4.1.

- **METACALIBRATION in ngmix:** We implemented the `METACALIBRATION`¹⁷ bootstrapper method, which is a wrapper class to run measurements in the `ngmix` package and was used to produce the weak lensing shape catalog in the DES Y3 analysis (Gatti et al. 2020). The `METACALIBRATION` process can be performed on single-epoch or coadd images in each bandpass. With this calibration method, we hope to significantly reduce some of the shear calibration bias T21 measured in order to make comparisons of effects contributing to the bias more realistic and meaningful as we explore future *Roman* pipeline development. The detailed overview of the `METACALIBRATION` bootstrapper method can be found in Sec. 2.

3.2 Simulated Weak Lensing Sample

The way galaxies are simulated in this paper resembles the one in T21. We briefly overview how the galaxy properties are assigned

¹⁵ <https://github.com/esheldon/psc>

¹⁶ <https://github.com/barnabytrowe/imcom>

¹⁷ Version 1.3.6 was used. <https://github.com/esheldon/ngmix/wiki/Metacalibration>

Measurement type	CPU runtime (hours)	Catalog disk size
single-band multi-epoch	3.7	3.9 GB
single-band coadd	2.9	3.8 GB
multi-band multi-epoch	4.8	3.8 GB
multi-band coadd	5.0	3.8 GB

Table 1. The runtime for a single CPU and disk size of the shape catalogs for different simulation runs. The runtime for multi-band measurements is slower due to having to copy, uncompress, and read from the three MEDS files (each 1GB compressed) for each bandpass. Runtime for coadd measurements also includes the postage-stamp coadding, which dominates the runtime over the metacal process. For comparison, the image generation of one SCA takes 1.8 CPU hours.

from the CANDELS catalog and the galaxy distributions are provided using the Buzzard simulation.

Among several galaxy properties, the morphological distributions are uniformly random (e.g., bulge/disk ratio), but the random intrinsic ellipticity distribution is appropriate to that expected from the data (e.g., the right ellipticity variance). The photometric, size, and redshift properties are all drawn consistently from the *Roman* weak lensing sample predictions based on the CANDELS measurements (Hemmati et al. 2019). Since this CANDELS-based catalog was designed to be the representative of the ultimate *Roman* weak lensing source sample, both the association of magnitude, size, and redshift for each individual object and the total distribution overall for our galaxies is consistent with what is expected for the *Roman* measurements. It is also worth mentioning that our input catalog is actually the distribution of a noisy selection that has cuts in size and signal-to-noise ($S/N > 18$) representative of the nominal selection of the *Roman* weak lensing sample (Doré et al. 2018).

As mentioned in the beginning of this section, we use the Buzzard simulation to distribute the galaxies. In our simulations, only the projected distribution is selected randomly to enable a realistic projected clustering signal. The Buzzard has an upper redshift limit of 2.5. While we simulate the full Buzzard images, we isolate object stamps and only the isolated object stamps are added to the full image which are eventually used in the shape measurement for this work.

This pre-selection of the galaxies ends up with the distribution that is close to the nominal weak lensing sample that we did not need to do a selection post-simulation.

3.3 Simulation Runtime, Data Products, and Data Access

The simulations here match those produced in T21, but with different true shear values and the updates mentioned in Sec. 3.1, and so information about processing and data volume prior to the processing additions described in this paper match that provided in App. D of T21. The runtime of the shape measurement per MEDS region in the simulations and data volume on disk of the full shape catalogs (5 METACALIBRATION catalogs for one of four shear sets) is summarized in Table 1 for each of the different simulation runs. The simulations are run on the Duke Compute Cluster¹⁸, with solid-state disks for the simulation I/O. The time it takes to process one MEDS file is shown in the table. The simulation is composed of a total of 480 MEDS files, for a total run time of about 2381 CPU hours for the multi-band coadd measurement.

¹⁸ <https://oit-rc.pages.oit.duke.edu/rcsupportdocs/dcc/>

3.4 Validations with Simple Simulations

In addition to the main, realistic simulation of the *Roman* reference HLIS survey, we also produce several sets of much faster, simple simulations to verify that there are no obvious fundamental sources of systematic biases using the METACALIBRATION method on undersampled space-based images. These simple simulations thus play a role in ruling out the sources of systematic biases that may a priori potentially be a problem in the use of METACALIBRATION with space-based images.

The fixed parameters for the simulations are listed in Table 2. We fix the original pixel scale of the *Roman*, bandpass and input galaxy size. With these parameters, we simulated images with varying galaxy model profile, PSF model profile, artificial shear, and background noise level, without any complications in the images and pipelines such as detector effects and coaddition. We first chose simple light profiles for galaxies and PSF to be Gaussian (with PSF half-light radius of 0.089 arcsec, which matches the expected average PSF size for H158 of 0.178 arcsec from T21), and verified with *Basic-0.02* simulation that our input gravitational shear ($|g|=0.02$) is unbiased in the METACALIBRATION framework and achieves the required multiplicative bias for *Roman*. Figure 1 shows that our choice of applied shear is below the shear requirement; therefore, it will not be the contributor to the bias in the other simulation variants or the full simulation. We also tested the same setup with different input shears (*Basic-0.05* and *Basic-0.1*) to test where the weak shear approximation breaks down. The values of inferred bias are shown in Table 3.

Next, we tested the shape measurement pipeline by doubling the background noise with *Doublesky-0.02*. This test should validate that the METACALIBRATION process can tolerate the induced correlation of Poisson noise in the object profiles during the METACALIBRATION shearing process, since it is not currently symmetrized in the process as the background noise field is (Sheldon & Huff 2017). We find that this result is also consistent with zero, so we can confirm that the treatment of correlated Poisson noise does not trigger any bias at the level we can probe with the current simulations.

In the final row in Table 3 (*RomanPSF-0.02*), we finally validate that the use of the complex *Roman* PSF instead of a Gaussian PSF does not bias the shape recovery even though it is undersampled. We note that these tests were performed before updating the PSF rotation, and so they do not benefit from rotationally-induced isotropy of the effective PSF. Since none of these obvious potential issues using simple Gaussian galaxy profiles will cause bias in m at the level we can probe in the more complex simulation, we can more easily interpret results of the more complicated simulation and analysis pipelines described in the following sections. However, there remains a potentially concerning non-zero additive bias in c_2 , particularly when using the *Roman* PSF model that will need to be studied further.

4 COADD AND SHEAR CALIBRATION PIPELINES

Our goal is to test whether the recovered shear with METACALIBRATION is non-biased for *Roman* and to understand the factors that might contribute to any non-negligible bias. In order to do so, we need to build measurement pipelines within the current simulation framework that produce a final calibrated shear measurement. In this section, we present in detail how coadd images are produced with psc from the undersampled single-epoch images and how METACALIBRATION is implemented to calibrate the measured shear.

Parameter	Value
Pixel scale	0.11 arcsec/pixel
Bandpass	H158
Galaxy half-light radius	1.0 arcsec
Stamp size	Multiples of 32 pixels each side

Table 2. List of the parameter choices for the simple simulations. For all the simple simulation runs, we used a Gaussian galaxy profile and the magnitude for each object is drawn randomly from the *CANDELS* catalog. For the stamp size, the multiplying factor was chosen so that 99.5% of the flux is in the stamp.

4.1 Postage Stamp Coadds

Coaddition is the process of summing information from multiple overlapping images. If the single-epoch images are dithered, a Nyquist-sampled image can be constructed out of multiple undersampled exposures of an object. While this process can also be beneficial in increasing the S/N value of an object and reducing the impact of pixel noise, several challenges need to be addressed for images taken with telescopes that can rotate. When rotation is introduced, this coadding process becomes more complex to interpolate the image to stack a pixel grid. While coaddition can introduce new challenges and potential biases due to the complexity of coadding the original PSF and its interpolation scheme, potential bias due to the undersampling of the original images can be mitigated by appropriately coadding dithered images.

Among imaging surveys, coadding a small region of the sky is common, for example *SWARP* (Bertin et al. 2002) or *DRIZZLE* (Fruchter & Hook 2002). However, we decided to coadd the postage-stamp cutouts to simplify the treatment of the coadd PSF. It is also beneficial to use this method because we need coadds which can be directly injected into the shape measurement pipeline in memory rather than written as images to disk due to the number of cutouts we have to process. We specifically use the simple interpolation-based coadding method using `GalSim`, `psc` (postage stamp coadds), as our coadding process. While this method does not explicitly account for undersampling of the images and will produce aliasing at some level, we find that this is not an important factor at our current precision of tests in this work. Future work will explore more principled methods like `IMCOM` (Rowe et al. 2011) that explicitly account for the undersampling of space-based imaging like our Roman image simulations.

We reconstruct a better-sampled coadd image from multiple exposures in MEDS files. For each exposure of the object we render the *Roman* PSF with a stamp size of 32 pixels at the galaxy centroid. This choice of stamp size ends up losing about 2-4% of the total flux of the PSF. However, we have no evidence that this impacts the shape measurement. We modified the original `psc` code to improve performance for this *Roman* study, and these modifications are explained below with the general coadding process in `psc`.

The algorithm:

- (i) Finds the WCS of the first exposure of the object.
- (ii) Translates the original WCS to a flat WCS (locally diagonal Jacobian representation), because it produces more stable results with `ngmix`.
- (iii) Creates the coadd stamp with $0.8 \times$ original pixel scale. We scale the original pixel scale of the final coadd stamp to increase

the image sampling. This final pixel scale was chosen to prevent the presence of visual artifacts in the structure of the coadd PSF image.

- (iv) Creates an interpolated image with `GalSim` using a `lanczos3` interpolant and sums them.
- (v) Creates a coadded noise image from the weight of the original images.

Figure 3 shows an example of the simulated single-epoch and coadded images and PSFs for objects with low and high S/N. Note that the shape and struts pattern in the original PSF can be isotropized by coadding the rotationally dithered PSFs.

Figure 4 shows the coadd products in different bandpasses for a relatively high S/N object.

4.2 Shape Calibration & Measurement with `ngmix`

Once we construct the individual galaxy stamp coadds from the MEDS files, we recover the calibrated shear signal using the `METACALIBRATION` process (Huff & Mandelbaum 2017; Sheldon & Huff 2017). In this work, the default interpolation kernel (`lanczos15`) was used to create the metacalibrated images, and the numerical tolerances used are also the default `GalSim` settings. The bootstrapper method used in `ngmix` wraps the `METACALIBRATION` and the shape fit processes. The priors used for the fit are listed in Table 4.

The deconvolution process in `METACALIBRATION` was performed using the coadded PSF that is still undersampled. Since having a matching pixel scale in the galaxy and PSF image is a requirement for the version of the `ngmix` pipeline we implemented, we were not able to oversample the simulated *Roman* PSF to utilize a more accurate PSF model. Future versions of these measurements should include the ability to provide a better-sampled PSF image for the deconvolution in the measurement. We also note that for the reconversion process in `METACALIBRATION` we have attempted the measurement with the `fitgauss`¹⁹ and `gauss` PSF model to reconvolve the sheared galaxy images, and the measurement with `fitgauss` model was numerically unstable resulting in the inconsistency between m_1 and m_2 . We, therefore, use the `gauss` model for the rest of the simulations.

The covariances are computed using the bootstrap estimate of standard error. From the observed ellipticity catalogs, we randomly choose n samples with replacement, where n is the length of the data set, and compute the distributions of multiplicative (f_i^m) and additive (f_i^c) bias for $i = 1, 2, 3, \dots, N$ (N is the number of times the resampling is carried out) in the same way as above. The distributions are then used to compute the error estimate,

$$\sigma_{N,f} = \sqrt{\frac{1}{N-1} \sum_{i=1}^N (f_i - \bar{f}_i)^2}, \quad (9)$$

where we use sample $N=200$.

5 RESULTS

In this section, we present the properties of the simulated data products and the shape measurement results from various simulation variants. We divide our shape measurement into two categories; single-band and multi-band. For single-band measurements, in each

¹⁹ An isotropic Gaussian PSF model fitted to the original PSF.

simulation variants	galaxy profile	PSF profile	shear	background noise level	$m_1 \times 10^2$	$m_2 \times 10^2$	$c_1 \times 10^4$	$c_2 \times 10^4$
Basic-0.02	Gaussian	Gaussian	0.02	5714.36 e-/arcsec ²	0.01±0.10	-0.02±0.10	-0.02±0.14	1.06±0.14
Basic-0.05	Gaussian	Gaussian	0.05	5714.36 e-/arcsec ²	0.23±0.07	0.22±0.07	0.05±0.33	1.08±0.33
Basic-0.1	Gaussian	Gaussian	0.1	5714.36 e-/arcsec ²	0.99±0.03	0.99±0.03	0.13±0.33	0.88±0.33
Doublesky-0.02	Gaussian	Gaussian	0.02	11428.72 e-/arcsec ²	-0.12±0.18	0.01±0.18	0.06±0.36	1.04±0.36
RomanPSF-0.02 (non-rotated)	Gaussian	Roman	0.02	5714.36 e-/arcsec ²	0.13±0.10	0.18±0.10	-0.02±0.19	5.33±0.19

Table 3. This table compares the shear calibration bias, both multiplicative and additive bias for different simple simulation runs. In each simulation except the first and last row, 5 million objects were simulated. We simulated 15 million objects for the first and last row to obtain sufficiently small uncertainties.

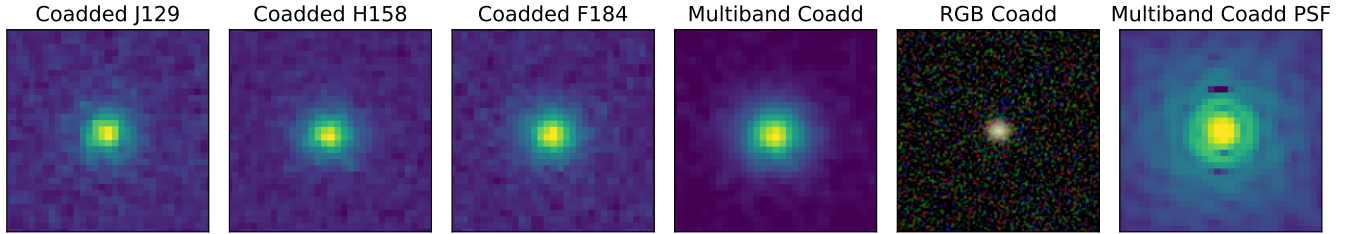


Figure 4. The left 3 panels show an example of the coadded galaxy images for each filter. The S/N for each filter is S/N=90, 68, 108, respectively. The 4th and 5th panels show the multi-band coadd images of the same object; each with linear scale and RGB scale. The S/N of the coadd image is S/N=110. Finally, the right-most panel shows the coadded multi-band PSF in a log scale. Some pixels with negative values were produced in the process of making the multi-band coadd PSF due to limitations in the fast interpolant functions used, but this has no impact on the results.

Parameter		Prior
Pixel centroid offset	Flat	$0 < p_{x,y} < 0.11$
Shear	Gaussian	$\langle g \rangle = 0.0, \sigma_{ g } = 0.3$
Galaxy size	Flat	$10^{-5} < T \text{ (arcsec}^2) < 10^4$
Flux fraction of the bulge	Gaussian	$\langle f \rangle = 0.5, \sigma_f = 0.1$
Total flux	Flat	$0 < F \text{ (ADU)} < 10^6$

Table 4. List of prior values and distributions used for the Gaussian mixture fit.

filter, we measured the shapes from the original single exposures by jointly fitting them: we call this single-band multi-epoch measurement. We also measured shapes with the single-band coadd in each filter: we call this single-band coadd measurement. For the multi-band multi-epoch measurement, we matched the objects between each filter and measured the shapes with the joint-fit of single exposures across all the filters. The multi-band coadd measurement was jointly fit across the three coadds from each filter to recover the shapes.

5.1 Statistics of the Shape Catalog

Galaxies that are simulated are pre-selected to meet the *Roman* Weak Lensing selection used for the mission requirements (Doré et al. 2018; Troxel et al. 2021). In total, the galaxy photometry catalog contains 907,170 galaxies and from this catalog we simulated galaxies on 18 SCAs across 198 pointings for F184, 227 pointings for H158, and 238 pointings for J129 bandpass. We did not make any selection cuts on the simulated catalogs based on measured properties, since all input objects are selected to pass requirements for weak lensing selection. In our samples, no de-blending was necessary since the shape measurement was performed on object stamps

without neighboring objects. Blending issues related to the object detection is mentioned later in Sec. 6.

In the end, we were able to measure the shapes of about 95% of all the objects in the photometry catalog in each filter. This 5% loss is mostly due to the fact that some objects are not saved in stamps due to being too large (i.e., require a stamp size of greater than 256 pixels). This selection is on the true size only, and so is not correlated with the shear. Some additional object shapes were not measured due to the Gaussian mixture fit in *ngmix* failing to converge. This also includes a very small number of objects that are rejected due to all cutouts being too near the SCA edges. The total number of the recovered objects for single-band measurements was, 861,407 for F184, 863,146 for H158, and 859,193 for J129. For the multi-band (H158+J129+F184) coadd measurements, we used objects that are measured successfully in all of the filters and the total number of the recovered objects is 851,821. Figure 5 shows the true magnitude and size, the measured signal-to-noise and size of galaxies in the METACALIBRATION shape catalogs. There is a significant boost in signal-to-noise in the multi-band catalog vs the single-band catalogs. While the measured size (T) does not agree well with the input size derived from the half-light radius, this is a known issue due to fitting a Gaussian model to a galaxy with size defined as part of a much more complex profile.

5.2 Shear Calibration Bias

We estimate the levels of shear calibration bias associated with calibrating shapes with METACALIBRATION in *Roman* images as described in Sec. 4.2. The multiplicative and additive bias values listed in the text are the average of m_1 and m_2 , and c_1 and c_2 . The comprehensive results can be found in Table 5 and Fig. 6 shows the single-band single exposures and coadd results compared. These multiple simulation variants were run to achieve three milestones. One is to

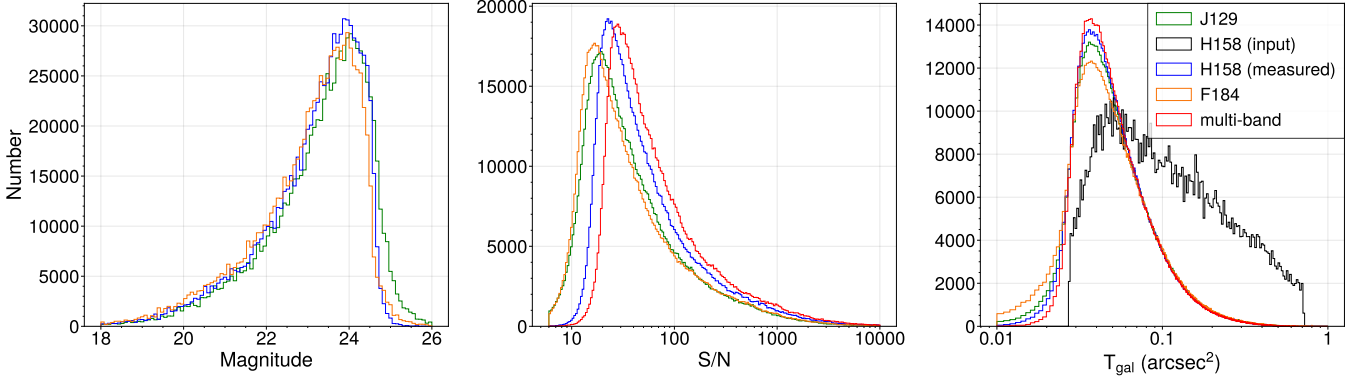


Figure 5. The histograms of input and measured galaxy properties in `ngmix` for single-band coadd and multi-band coadd measurements. **Left:** the input magnitudes of galaxies for all three filters we have used to measure shapes. The mean magnitude for J129, H158, F184 are respectively 23.3, 23.1, 23.0. **Middle:** the signal-to-noise ratio of the single-band and multi-band coadds. The median S/N for J129 and multi-band are respectively 29, 39, 27, and 50. **Right:** the input galaxy size for H158 approximated using a Gaussian profile with the half-light radius in the input H158 catalog, and the measured galaxy size T for the single-band and the multi-band coadd in units of arcsec^2 . The mean size for input and measured galaxies are 0.15 and 0.09 arcsec^2 for H158. The measured size is the size of the best fit Gaussian (maximum likelihood in this case) and it is not expected to match with the true size based on the half-light radius of the nominal (non-Gaussian) profiles.

characterize how much the shear bias exists if we were to use the original, undersampled images, by recovering shears from the single exposures in each bandpass. Second is to verify if coadding can mitigate the effect of undersampling. Lastly, as the final assessment we investigate how combining the three bandpasses can result in better constraining the recovered shear.

For the single-band measurements, we can use the sampling factor defined in Equation (2) per bandpass to show the relationship between the shear bias and image sampling. The sampling factor is an indication of how undersampled the image is in each bandpass. The sampling factor for each single-band measurement can be found in Table 5. This relationship between sampling factor and shear bias was previously explored in K21 using *Euclid* simulation with different shape measurement algorithms, where they found that the estimated multiplicative bias has a relatively large dependence on the sampling factor. Their result can be extrapolated to our single-band multi-epoch results. The multiplicative bias of single-band multi-epoch measurements is consistent with zero within 2σ in each filter, with mean uncertainty $\sigma_m=0.72\%$, except for $m_2 = (-1.61 \pm 0.66)\%$ in H158, which is slightly larger. This level of bias is consistent with the finding from K21.

When the coadded images for each filter are used, the recovered multiplicative shear bias is about half the multi-epoch cases, and is consistent with zero at the $\sim 1\sigma$ level. The additive bias remains at a similar level within uncertainties.

Finally, we discuss the results with multi-band measurements. We performed multi-band measurements with the three filters used in the previous measurements. One multi-band measurement used all of the single epoch images from all the filters and jointly fit the shape of the galaxy. The multiplicative and additive bias is, respectively, $m = (-0.76 \pm 0.43)\%$ and $c = (2.56 \pm 0.79) \times 10^{-4}$. This result generally agrees with the single-band multi-epoch measurements, and is consistent with zero bias at the $\sim 2\sigma$ level. The other measurement is performed as a joint-fit across the coadd images for each filter. The multiplicative and additive bias is, respectively, $m = (-1.13 \pm 0.60)\%$ and $c = (2.38 \pm 1.24) \times 10^{-4}$. These results are again consistent with zero at the 2σ level, but have a large uncertainty relative to the Roman mission requirements. Scaling simply by volume, assuming a Gaussian error distribution, we would need a significantly larger

simulation volume of about 2000 deg^2 in this complex simulation mode to draw firm conclusion about the performance of multiband measurements. This is comparable to the area of the reference Roman survey.

To further explore the shape catalogs, we performed a set of basic null tests and show representative results for e_1 for the H158 multi-epoch and coadd catalogs, and multi-band coadd catalog. The null tests should show that the mean shear residual ($\langle \Delta e_1 \rangle$) is zero (flat as a function of galaxy properties) in the absence of any systematic biases. Figure 7 shows the relationship between the mean shear and several input and measured properties of galaxies for all the measurement cases. We find no significant trends in mean shear vs. galaxy properties or vs PSF properties, which are not included in the figure.

6 FUTURE SIMULATION NEEDS AND PLAN

We have investigated how `METACALIBRATION` handles the complex *Roman* PSF and undersampled images without accounting for the effect of blending. However, it has been found that galaxy blending at different redshifts could introduce a significant shear-dependent detection bias when calibrated with `METACALIBRATION` (e.g., Sheldon et al. 2020, MacCrann et al. 2020). In future studies, we will investigate the impact of blending in *Roman* image simulations and implement an extended pipeline to correct shear-dependent blending/detection biases (e.g., `METADETECTION`) to explore more realistic shear calibration for the real survey.

Our team continues to increase the realism of the image simulations for future weak lensing calibration analyses. In the next generation of these simulations, we expect to include the following updates or upgrade these parts of the simulation.

- **Simulation Volume:** Expand the simulated area by a factor of four to 20 deg^2 , in order to obtain smaller error bars on the resulting shear calibration biases. Increasing the simulation volume has additional benefits beyond a more precise bias estimate, such as the ability to calibrate spatial dependence of shear and to measure two-point correlation function and propagate the biases into a cosmological analysis.

simulation variants	sampling factor (Q)	$m_1 \times 10^2$	$m_2 \times 10^2$	$c_1 \times 10^4$	$c_2 \times 10^4$
single-band multi-epoch (J129)	0.88	1.17 ± 0.68	0.44 ± 0.75	4.46 ± 1.32	0.64 ± 1.31
single-band multi-epoch (H158)	1.08	-1.07 ± 0.62	-1.61 ± 0.66	2.83 ± 1.35	2.33 ± 1.22
single-band multi-epoch (F184)	1.31	-0.86 ± 0.72	-0.69 ± 0.83	2.62 ± 1.56	0.23 ± 1.53
single-band coadd (J129)	1.10	-0.59 ± 0.68	-0.94 ± 0.64	4.91 ± 1.46	1.78 ± 1.17
single-band coadd (H158)	1.35	-0.69 ± 0.63	-0.83 ± 0.61	2.16 ± 1.31	0.77 ± 1.19
single-band coadd (F184)	1.64	0.37 ± 0.83	0.10 ± 0.75	2.22 ± 1.46	0.08 ± 1.58
multi-band multi-epoch	N/A	-0.68 ± 0.59	-0.85 ± 0.58	3.09 ± 1.21	2.04 ± 1.11
multi-band coadd	N/A	-1.02 ± 0.62	-1.24 ± 0.57	2.37 ± 1.26	2.38 ± 1.22

Table 5. A comparison of the shear calibration bias, both multiplicative and additive bias, for different simulation runs.

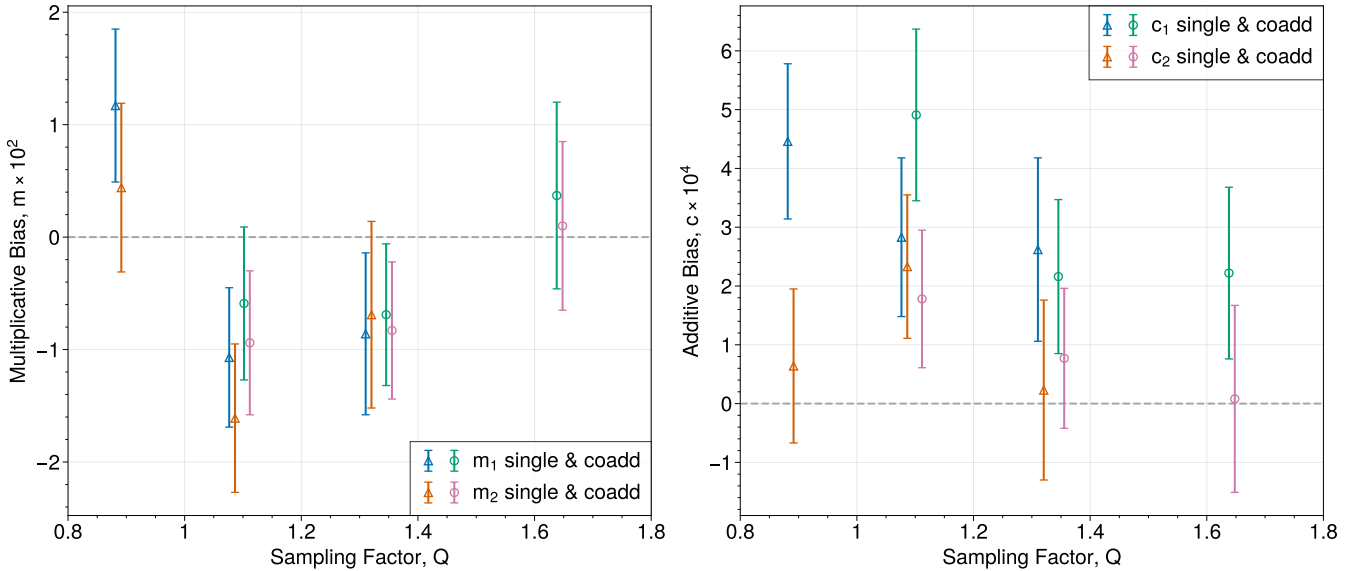


Figure 6. The multiplicative ($m \times 10^2$) (left) and additive ($c \times 10^4$) (right) bias of the single-band multi-epoch and coadd measurements. From the left to the right data points, they represent the data for each of the J129 multi-epoch, H158 multi-epoch, J129 coadd, F184 multi-epoch, H158 coadd and F184 coadd measurements. The data points for the m_2 and c_2 measurements are shifted by +0.01 for visual clarity. The non-calibrated results from the first-generation of the simulations by T21 were $m_1 = (-7.56 \pm 0.19)\%$, $m_2 = (-9.49 \pm 0.19)\%$ and $c_1 = (1.20 \pm 0.17) \times 10^{-3}$, $c_2 = (-1.57 \pm 0.16) \times 10^{-3}$. We can conclude that our calibration bias is an order of magnitude smaller than the previous versions of the simulations, and comparable or smaller than the bias-level seen in the Stage-III surveys.

- **Pixel Masks:** Future versions of the simulations will take into account complex pixel masking of detector non-idealities, such as hot or dead pixels. This masking will be propagated through the analysis to provide realistic masking challenges.

- **Near-Infrared Detector Effects:** Incorporate more realistic detector effects as measured in tests on the flight detectors (Mosby et al. 2020) and produce two versions of the simulation with and without them to determine the impact on the final cosmology result. The detector effects that are not simulated in this paper but will be incorporated are relative quantum efficiency, quantum yield, charge diffusion, brighter-fatter effect, burn-in, count rate non-linearity, classical non-linearity, vertical trailing pixel effect, bad pixels, gain, and the bias frame.

- **Image Coaddition:** As one of the scene coadd algorithms, we will implement a new coaddition strategy that coadds the whole

scene instead of individual stamp cutouts using AstroDrizzle²⁰: A Python implementation of MultiDrizzle which was used for Hubble Space Telescope (Brammer et al. 2003). With AstroDrizzle, we are able to further mitigate the effect of undersampling in the Roman images with smaller coadd pixel scales. We expect this to further reduce the measured shear bias based on its trend with sampling factor. As a more mathematically-principled method that directly accounts for the undersampling of the images, we can also evaluate the use of the IMCOM algorithm (Rowe et al. 2011) in the future.

- **Source Detection:** Implement a source detection and deblending methodology to allow more realistic tests of shear recovery.

- **Selection Cuts:** Simulate objects to below the detection threshold of the survey and incorporate standard quality assurance cuts (e.g., S/N) on the shape catalog.

²⁰ <https://github.com/spacetelescope/drizzlepac>

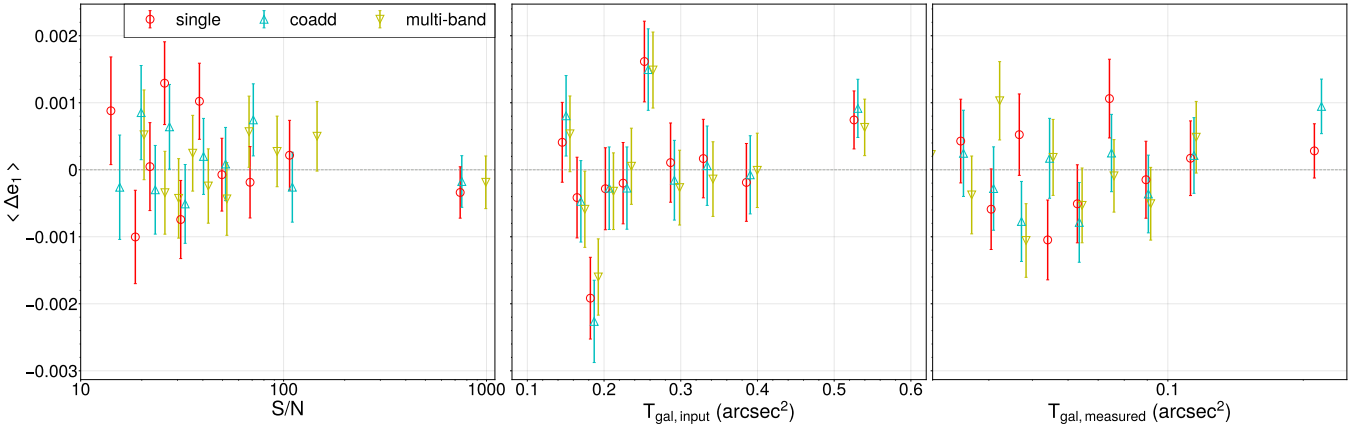


Figure 7. The mean shear residual ($\langle \Delta e_1 \rangle$; $\langle e_{1,\text{measured}} \rangle - \langle e_{1,\text{expected}} \rangle$) as a function of various properties of galaxies for H158 single-band multi-epochs, coadds, and multi-band measurements. We are only showing the e_1 residual because e_2 showed similar behaviors in each test. We find results that are consistent with a null signal for signal-to-noise (left), true galaxy size (middle), and measured galaxy size (right). The mean shear is computed with the shear response and selection response in each bin to account for the selection bias. To make the figure more visible, blue points are shifted by -1.0 in S/N , -0.005 in $T_{\text{gal, input}}$, -0.001 in $T_{\text{gal, measured}}$, and yellow points are shifted by $+1.0$ in S/N , $+0.005$ in $T_{\text{gal, input}}$, $+0.001$ in $T_{\text{gal, measured}}$.

7 CONCLUSIONS

In this paper, we explored the performance of the METACALIBRATION shape measurement calibration algorithm and presented the first shear calibration result without the effect of blending on a realistic simulated version of the reference *Roman* HLIS. Accurately characterizing how much shear estimates are biased using realistic simulated survey images is a requirement to successfully complete the weak lensing program of the *Roman* HLIS. This early work allows us to develop such simulation resources and to benchmark current weak lensing methods to explore where effort is still needed in development for the *Roman* mission.

In a larger suite of simple simulations, where the galaxy and PSF profiles are Gaussian, we find that the shear calibration bias using METACALIBRATION is consistent with zero at the 0.1% level, even though the images are undersampled. This finding persists even when using an accurate, complex *Roman* PSF model. When exploring the performance of METACALIBRATION in the current simulation framework where realistic complexities are incorporated, the runtime cost is significantly increased, and we can only constrain the shear calibration bias at the 0.6% level. In these simulations we include coadding the single-epoch cutout images and fitting the shapes from multiple bandpasses, and we find that shear estimates with METACALIBRATION are unbiased at the $\sim 2\sigma$ level, which is similar to current-survey constraints. At the original image sampling level, the trend in bias vs sampling factor Q is similar to what was previously found for METACALIBRATION bias on undersampled images in the study by K21 using image simulations built for *Euclid*, but at lower levels of bias. By coadding the cutout images and increasing the image sampling factor, we find that the residual bias is reduced by about a factor of two, but this is similar to the uncertainty. However, this is a promising result for using coadd-level shape measurement for *Roman*, and we plan to further investigate the use of METACALIBRATION with image coadds that can reconstruct Nyquist-sampled images in all bandpasses in future work.

These results are currently limited by the available simulation volume in the realistic simulated survey. To further constrain the shear calibration bias and validate that the *Roman* mission will be able to achieve the weak lensing calibration required for the survey,

we have outlined in Sec. 6 a variety of simulation improvements being planned in future versions of the *Roman* simulations that are currently being developed, including an exploration of the impact of blending and object detection on the calibration. We will also need to simulate much larger volumes of data, which is a significant challenge in terms of computing resources and storage space. The next version of the realistic simulation will cover about a factor of four more of the sky. These first results with METACALIBRATION in realistic simulated *Roman* HLIS imaging demonstrate that the METACALIBRATION shear calibration approach is a feasible strategy for the *Roman* mission and undersampled imaging more generally. However, significant additional work to study shear calibration in the presence of blending and at significantly larger survey volumes is essential for reaching the precise requirements for the *Roman* weak lensing mission.

8 ACKNOWLEDGEMENTS

We thank Matthew Becker and Erin Sheldon for the useful discussions on the use of `ngmix`, and Arun Kannawadi for discussions about related *Euclid* shape measurement work. This work was supported by NASA Grant 15-WFIRST15-0008 as part of the Roman Cosmology with the High-Latitude Survey Science Investigation Team (<https://www.roman-hls-cosmology.space/>). This work used resources from the Duke Compute Cluster.

DATA AVAILABILITY

The new measurement catalogs produced in this work are available on reasonable request to the authors.

REFERENCES

- Aihara H., et al., 2018, *PASJ*, 70, S4
- Albrecht A., et al., 2006, arXiv e-prints, [pp astro-ph/0609591](https://arxiv.org/abs/astro-ph/0609591)
- Asgari M., et al., 2021, *A&A*, 645, A104
- Bartelmann M., Schneider P., 2001, *Phys. Rep.*, 340, 291

- Brammer G., Koekemoer A. M., Kiziltan B., 2003, in HST Calibration Workshop : Hubble after the Installation of the ACS and the NICMOS Cooling System. p. 325
- Bridle S., et al., 2010, *MNRAS*, **405**, 2044
- Brout D., et al., 2022, arXiv e-prints, p. [arXiv:2202.04077](https://arxiv.org/abs/2202.04077)
- Choi A., Hirata C. M., 2020, *PASP*, **132**, 014502
- DES Collaboration Abbott T. M. C., et al., 2022, *Phys. Rev. D*, **105**, 023520
- DeRose J., et al., 2019, arXiv e-prints, p. [arXiv:1901.02401](https://arxiv.org/abs/1901.02401)
- Dodelson S., 2017, Gravitational Lensing
- Doré O., et al., 2018, arXiv e-prints, p. [arXiv:1804.03628](https://arxiv.org/abs/1804.03628)
- Fruchter A. S., Hook R. N., 2002, *PASP*, **114**, 144
- Gatti M., et al., 2020, arXiv e-prints, p. [arXiv:2011.03408](https://arxiv.org/abs/2011.03408)
- Giblin B., et al., 2021, *A&A*, **645**, A105
- Gil-Marín H., et al., 2020, *MNRAS*, **498**, 2492
- Górski K. M., Hivon E., Banday A. J., Wandelt B. D., Hansen F. K., Reinecke M., Bartelmann M., 2005, *ApJ*, **622**, 759
- Grogin N. A., et al., 2011, *ApJS*, **197**, 35
- Hemmati S., et al., 2019, *ApJ*, **877**, 117
- Heymans C., et al., 2006, *MNRAS*, **368**, 1323
- Hoekstra H., Viola M., Herbonnet R., 2017, *MNRAS*, **468**, 3295
- Huff E., Mandelbaum R., 2017, arXiv e-prints, p. [arXiv:1702.02600](https://arxiv.org/abs/1702.02600)
- Huterer D., Takada M., Bernstein G., Jain B., 2006, *MNRAS*, **366**, 101
- Ivezic Ž., et al., 2019, *ApJ*, **873**, 111
- Jarvis M., et al., 2016, *MNRAS*, **460**, 2245
- Kannawadi A., Rosenberg E., Hoekstra H., 2021, *MNRAS*, **502**, 4048
- Kilbinger M., 2015, *Reports on Progress in Physics*, **78**, 086901
- Kitching T. D., et al., 2013, *ApJS*, **205**, 12
- Koekemoer A. M., et al., 2011, *ApJS*, **197**, 36
- LSST Science Collaboration et al., 2009, arXiv e-prints, p. [arXiv:0912.0201](https://arxiv.org/abs/0912.0201)
- Laureijs R., et al., 2011, arXiv e-prints, p. [arXiv:1110.3193](https://arxiv.org/abs/1110.3193)
- Lin C.-H., Mandelbaum R., Troxel M. A., Hirata C. M., Jarvis M., 2021, arXiv e-prints, p. [arXiv:2106.10273](https://arxiv.org/abs/2106.10273)
- MacCrann N., et al., 2020, arXiv e-prints, p. [arXiv:2012.08567](https://arxiv.org/abs/2012.08567)
- Mandelbaum R., 2018, *ARA&A*, **56**, 393
- Mandelbaum R., et al., 2015, *MNRAS*, **450**, 2963
- Mandelbaum R., et al., 2018, *MNRAS*, **481**, 3170
- Massey R., et al., 2007, *MNRAS*, **376**, 13
- Mosby G., et al., 2020, *Journal of Astronomical Telescopes, Instruments, and Systems*, **6**, 046001
- Perlmutter S., Riess A., 1999, in Caldwell D. O., ed., American Institute of Physics Conference Series Vol. 478, COSMO-98. pp 129–142, [doi:10.1063/1.59382](https://doi.org/10.1063/1.59382)
- Planck Collaboration et al., 2020, *A&A*, **641**, A8
- Pujol A., Kilbinger M., Sureau F., Bobin J., 2019, *A&A*, **621**, A2
- Riess A. G., et al., 1998, *AJ*, **116**, 1009
- Rowe B., Hirata C., Rhodes J., 2011, *ApJ*, **741**, 46
- Rowe B. T. P., et al., 2015, *Astronomy and Computing*, **10**, 121
- Shapiro C., Rowe B. T. P., Goodsall T., Hirata C., Fucik J., Rhodes J., Seshadri S., Smith R., 2013, *PASP*, **125**, 1496
- Sharma S., Bland-Hawthorn J., Johnston K. V., Binney J., 2011, *ApJ*, **730**, 3
- Sheldon E. S., 2014, *MNRAS*, **444**, L25
- Sheldon E. S., Huff E. M., 2017, *ApJ*, **841**, 24
- Sheldon E. S., Becker M. R., MacCrann N., Jarvis M., 2020, *ApJ*, **902**, 138
- Spergel D., et al., 2015, arXiv e-prints, p. [arXiv:1503.03757](https://arxiv.org/abs/1503.03757)
- Tamone A., et al., 2020, *MNRAS*, **499**, 5527
- The Dark Energy Survey Collaboration 2005, arXiv e-prints, p. [astro-ph/0510346](https://arxiv.org/abs/astro-ph/0510346)
- Troxel M. A., et al., 2021, *MNRAS*, **501**, 2044
- Zonca A., Singer L. P., Lenz D., Reinecke M., Rosset C., Hivon E., Gorski K. M., 2019, *Journal of Open Source Software*, **4**, 1298
- Zuntz J., et al., 2018, *MNRAS*, **481**, 1149
- de Jong J. T. A., Verdoes Kleijn G. A., Kuijken K. H., Valentijn E. A., 2013, *Experimental Astronomy*, **35**, 25
- Hoekstra, Henk and Kannawadi, Arun and Kitching, Thomas D., 2021, *A&A*, **646**, 124

This paper has been typeset from a $\text{\TeX}/\text{\LaTeX}$ file prepared by the author.